Computers and Geotechnics 159 (2023) 105428

Contents lists available at ScienceDirect

Computers and Geotechnics

journal homepage: www.elsevier.com/locate/compgeo

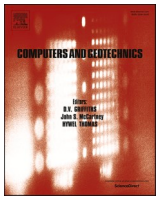

Impact of hyper-elasticity on cyclic sand modelling: A numerical study based on SANISAND-MS

Hongjian Lan [a], Haoyuan Liu [b,*], Hongfen Zhao [a,*]

[a] School of Civil Engineering, Sun Yat-sen University, Zhuhai 519082, China
[b] Advanced Geomodelling Section, Norwegian Geotechnical Institute, Norway

ARTICLE INFO

Keywords:
Constitutive model
Ratcheting
Hyperelasticity
Hypoelasticity
Sand
Cyclic loading

ABSTRACT

Accurate simulation of foundation response subjected to repeated loading require reliable sand constitutive models to reproduce realistic sand cyclic behaviour. Many elastoplastic constitutive models adopted the hypo-elasticity law, which results in physically inaccurate strain accumulation prediction of soil when subjected to elastic cyclic loading. To address this issue, the existing elastoplastic bounding surface model SANISAND-MS has been upgraded with a hyperelastic formulation that is derived from the Helmholtz free energy function. The complete form of the derived nonlinear elasticity functions enhanced by stress induced anisotropy is presented in this work. The calibration of the upgraded SANISAND-MS is briefly discussed. It is demonstrated that the hyperelastic formulation with volumetric-deviatoric coupling: (1) guarantees no accumulation of elastic strain upon elastic cyclic loading, and (2) captures the stress-induced anisotropy of sand under reverse loading. This upgraded SANISAND-MS model with a physical adaptation and thermodynamically consistent elasticity law can predict strain accumulation accurately and is physically appropriate. Moreover, the upgraded SANISAND-MS is suitable for simulating problems with high-cyclic loads and is able to be used in boundary value problem simulations in areas including offshore engineering and railway engineering.

1. Introduction

Mobilization of small strain response of soil is widely encountered in geotechnical problems, such as offshore wind turbine foundations (Oh et al., 2018) and railway engineering (Debnath et al., 2022). There are two circumstances associated with small strain states in offshore foundations. The first is related to foundations subjected to high-cyclic loading with very small amplitudes, where limited irreversible cyclic strain is developed. The other is that during cyclic loading, upon unloading, the stress state evolution is reversed, and the soil behaves elastically. Determining parameters related to the small strain behaviour, such as initial stiffness and shear modulus, is critical in practice-oriented numerical analysis (Lashkari, 2010; Kallehave et al., 2012; Oh et al., 2018; Liu and Kaynia, 2021). Linear elasticity is the most direct way to represent the small strain mechanical behaviour of soil in the elastic domain at small strains. Nonlinear and anisotropic behaviour in elastic deformation with small shear stresses (Einav, 2012) has usually been overlooked. However, considering the nonlinear and anisotropic elasticity in the range of small strains is an important issue when predicting sand ratcheting for offshore foundations under serviceability conditions.

There are various advanced elastoplastic constitutive models capable of modeling soil behaviour across a wide range of strains, which is essential for a complete analysis of geotechnical problems. For clay monotonic behaviour simulations, Yao et al. (2009) developed a unified hardening (UH) model which can well capture various clay mechanical behaviours including strain hardening and strain softening, shear-induced dilatancy and stress path dependent features. The UH model provides a flexible and efficient model framework that allows easy modifications to achieve behaviour-specific improvement. Yao et al. (2019) developed CSUH based on the UH model framework. The CSUH model is the first unified model that can accurately predict both sand and clay monotonic behaviour.

For predicting the cyclic response of sands under long lasting cyclic loading, Dafalias and Manzari (2004) developed the critical state SANISAND04 model to reproduce fabric effects relevant to cyclic soil response. Following SANISAND04, many other SANISAND models have been developed (Taiebat and Dafalias, 2008; Lashkari, 2010) for

* Corresponding authors at: Advanced Geomodelling, Norwegian Geotechnical Institute, Oslo, Norway (H. Liu). School of Civil Engineering, Sun Yat-Sen University, Guangzhou 510275, China (H. Zhao).
E-mail addresses: haoyuan.liu@ngi.no (H. Liu), zhaohf7@mail.sysu.edu.cn (H. Zhao).

https://doi.org/10.1016/j.compgeo.2023.105428
Received 21 November 2022; Received in revised form 27 February 2023; Accepted 23 March 2023
Available online 5 May 2023

different purposes. Tasiopoulou and Gerolymos (2016) built the so-called 'Ta-Ger' model based on a framework that combines the theories of perfect elastoplasticity and smooth hysteresis. The model is able to predict sand cyclic behaviour including cyclic liquefaction and cyclic mobility. Liu et al. (2019) and Liu et al. (2020) considered the load induced anisotropy of sand and proposed a memory-enhanced SANISAND-MS model to be able to accurately predict sand ratcheting behaviour under various loading paths. The elastic behaviour of many elasto-plastic constitutive models is assumed to be linear isotropic or obeys a hypoelasticity law derived from empirical formulations. A typical hypoelasticity law proposed by Richart et al. (1970) was adopted by many elasto-plastic constitutive models (Li and Dafalias, 2001; Dafalias and Manzari, 2004; Taiebat and Dafalias, 2008; Lashkari, 2010). The law is achieved by adopting the linear Hooke's law with the development of tangent shear modulus over the variation of void ratio and confining pressure. However, the formulation of such an elasticity framework is proven to violate the first law of thermodynamics, the large accumulated residual strain is observed in the soil element even subjected to elastic cyclic loading (Simo and Pister, 1984; Lin, 2003; Xiao et al., 2005; Einav, 2012; Korobeynikov, 2019). Thus, the use of the incorrect physical hypoelastic relationship may result in a non-conservative response and inevitably accumulate elastic deformation energy under high-cyclic loads, which should be corrected in the model formulation for physical adaptation.

Differing from hypoelastic laws, hyperelasticity is a convenient approach to modeling the reversible behavior of soils with thermodynamic consistency. Many hyperelasticity models have been proposed in the literature. Some of these models are attempted to account for the features of pressure dependency and anisotropy in soils at the reversible regime. Gajo and Bigoni (2008) considered two varying exponents (denoted by l and n in their works) to describe the soil's nonlinearity and constructed a nonlinear anisotropic hyperelasticity law from a free energy function. The model is able to capture the soil's anisotropy behavior but could result in development of Poisson's ratio with different stress states under some specific conditions as proven by Amorosi et al. (2020). Cudny and Partyka (2017) developed a nonlinear isotropic hyperelastic model by incorporating a second-order fabric tensor to the complementary function proposed by Vermeer (1982). However, the model can only account for the transverse isotropic behavior of soils.

Einav and Puzrin (2004) investigated the consequences of combing conventional hypoelasticity law (energy non-conservative elasticity) and hyperelasticity law (energy conservative elasticity) within a plasticity framework. The models had been applied to study the effects of elasticity law on the real boundary value problem simulations. It concluded that significant effect on the accuracy of the model predictions can be found in tunnel excavation problem. Such a study puts emphasis on the importance of selecting theoretically rigorous and practically accurate elasticity law in geotechnical engineering problem studies. Despite the exploration of the elasticity law effects on object monotonic behaviour, few works focus on the effects on the cyclic perspective (for instance, the cyclically loaded offshore foundations).

Recently, a memory-enhanced constitutive model for sand, SANISAND-MS, has been developed to capture the ratcheting effects in sands that occur in high-cyclic loading (Liu et al., 2019, Liu et al., 2020). SANISAND-MS model is an elasto-plastic model based on bounding surface theory and a critical state framework. The model takes into account the effects of soil fabric and it evolves on sand cyclic behaviour through the so-called 'memory surface'. The model is proven to be capable of reproducing the representative, both monotonic and cyclic behaviour of sand. This model has been successfully implemented in the OpenSees Software to support the cyclic analysis of offshore foundations. However, the hypoelasticity law adopted in the model may result in less accurate strain accumulation in high cyclic loading simulations (Houlsby et al., 2005). It will consequently influence the accuracy of finite element simulation when applying the model to real boundary problem simulations. It is pertinent to modify the elastic relationship and consider the elastic energy conservation inside the yield locus to more robustly predict the strain accumulation.

The objective of this work is to employ a physically consistent elasticity theory – hyperelasticity law in the well accepted bounding surface plasticity models. This is achieved by replacing the original hypoelasticity law in the original SANISAND-MS model with a hyperelasticity theory proposed by Houlsby et al. (2019). Parameter calibrations of the upgraded model will be conducted. Monotonic and cyclic performance regarding the diversity of initial confining pressures, void ratios, and cyclic amplitudes will be presented against the experimental data and the original SANISAND-MS model. Moreover, the effects of the changing elasticity on the unloading responses and soil behaviour subjected to a closed elastic stress path will be discussed from a qualitative perspective.

2. Hyperelastic upgrade and calibration of SANISAND-MS model

In this work, the geotechnical sign convention (positive for compression) is assumed and the summation convention is adopted. Tensors are written in component-free boldface. Considering the Cartesian basis $\boldsymbol{e}_i$, $\boldsymbol{e}_j$, $\boldsymbol{e}_k$ and $\boldsymbol{e}_l$, two arbitrary second-order tensors $\mathbf{b}$ and $\mathbf{c}$ can be written as $\mathbf{b} = b_{ij}\boldsymbol{e}_i\boldsymbol{e}_j$ and $\mathbf{c} = c_{kl}\boldsymbol{e}_k\boldsymbol{e}_l$, respectively. The tensor operation signs $\otimes$ and $\overline{\otimes}$ can be defined as $\mathbf{b}\otimes\boldsymbol{c} = b_{ij}c_{kl}\boldsymbol{e}_i\boldsymbol{e}_j\boldsymbol{e}_k\boldsymbol{e}_l$ and $\mathbf{b}\overline{\otimes}\boldsymbol{c} = b_{ik}c_{jl}\boldsymbol{e}_i\boldsymbol{e}_j\boldsymbol{e}_k\boldsymbol{e}_l$, respectively. The trace of a tensor (for instance, $\mathbf{b}$) is denoted by $\mathrm{tr}()$ (thus the trace of $\mathbf{b}$ can be written as $\mathrm{tr}(\mathbf{b}) = b_{ii}$). The inner product of $\mathbf{b}$ and $\mathbf{c}$ is defined by $\mathbf{bc} = b_{ik}c_{kj}\boldsymbol{e}_i\boldsymbol{e}_j$. The colon ":" stands for the double product of two tensors. For the second order tensor calculations, the double product returns the trace of the product of the two second order tensors. For example, $\mathbf{b} : \mathbf{c} = \mathrm{tr}(\mathbf{bc})$. The second-order identity tensor $\mathbf{I}$ is defined as $\mathbf{I} = \delta_{ij}\boldsymbol{e}_i\boldsymbol{e}_j$, where δ_{ij} indicates the Kronecker delta. Fourth-order tensors are written in double-line boldface, e.g. the stiffness tensor $\mathbb{D}$.

Effective stress in the geotechnical convention is represented by adding a prime to a stress component (stress state). However, in this work, all stress states are effective, and primes are therefore skipped for simplicity. The strain tensor ε and effective stress tensor σ can consequently be defined as $\varepsilon = \mathbf{e} + 1/3\mathrm{tr}(\varepsilon)\mathbf{I}$ and $\sigma = \mathbf{s} + 1/3\mathrm{tr}(\sigma)\mathbf{I}$, where $\mathbf{e}$ is deviatoric strain tensor and $\mathbf{s}$ stands for deviatoric stress tensor. The superscript sym of a second-order tensor indicates the symmetrized tensor, i.e., $\varepsilon^{\mathrm{sym}} = 1/2(\varepsilon + \varepsilon^{\mathrm{T}})$, where the superscript T represents transposition. The invariants involved in this study include the mean effective stress $p = 1/3\mathrm{tr}(\sigma)$, deviatoric stress $q = \sqrt{3/2\mathrm{tr}(\mathbf{s}^2)}$, volumetric strain $\varepsilon_{\mathrm{v}} = \mathrm{tr}(\varepsilon)$, and deviatoric strain $\varepsilon_q = \sqrt{2/3\mathrm{tr}(\mathbf{e}^2)}$. The subscript in denotes the initial value of a quantity, e.g., e_{in} stands for the initial void ratio. E and C represent elastic strain energy and complementary energy functions, respectively.

2.1. Inclusion of a hyperelastic law

SANISAND-MS model (Liu et al., 2019) is an elasto-plastic model built based on the bounding surface plasticity theory and critical state framework. SANISAND-MS model includes three loci (Fig. 1): (a) a narrow conical yield locus (f); (b) a wide conical bounding locus (f_{b}); (c) a conical memory surface (f_{m}). Fabric related effects to sand high-cyclic behaviour are taken into account by the so-called 'memory surface'. The model performs well in capturing soil high-cyclic element test response under varying stress levels, relative densities and initial confining pressures.

In the SANISAND-MS model, the hypoelasticity law proposed by Richart et al. (1970) is adopted to simulate the sand behaviour inside the yield locus (f). The stiffness tensor is computed with Hooke's law. The shear and bulk moduli (G and K) vary with void ratios and confining pressures (Richart et al., 1970; Li and Dafalias, 2002) in the forms:

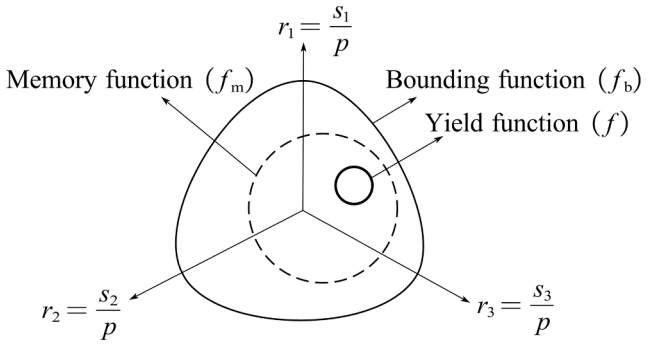

Fig. 1. Relevant loci in the deviatoric stress ratio plane (modified after Liu et al., 2019).

$$G = G_0 p_{at} \frac{(2.97 - e)^2}{1 + e} \left(\frac{p}{p_{at}}\right)^{\frac{1}{2}} \tag{1}$$

$$K = \frac{2(1+\nu)}{3(1-2\nu)} G \tag{2}$$

In the equations, G_0 is a dimensionless shear stiffness parameter; p_{at} is the reference atmospheric pressure; e and p represent the current void ratio and the mean effective stress, respectively; ν is Poisson's ratio.

The relationships defined by Eqs. (1) and (2) cannot guarantee the fully recoverable elastic behaviour of a material under closed elastic load paths (Zytynski et al., 1978). Thus, it might violate the law of thermodynamics. Such a statement can be visualized in Fig. 2. A closed pure elastic loading path (A1)-(A2)-(A3)-(A4)-(A5) in triaxial stress space is applied (see Fig. 2(a)). The material is first subjected to an increase in deviatoric stress q at constant mean effective stress p, from point A1 to point A2, followed by an increase in p at constant q until point A3. Under constant p from point A3, the deviatoric stress q is reduced until point A4. In the final stage, the mean effective stress is reduced so that the stress state returns to its initial value at point A1. This closed elastic stress path is designed to demonstrate a reversible process. The corresponding responses of deviatoric stress versus deviatoric strain (B1-B5), volumetric strain versus deviatoric strain (C1-C5) and mean effective stress versus volumetric strain (D1-D5) for this stress path are depicted in Fig. 2(b), Fig. 2(c) and Fig. 2(d), respectively.

It is well recognised that elastic materials accumulate no deformation after the applied load is removed. However, as shown in Fig. 2(b), the non-closed deviatoric strain ε_q loop (point B5 is different from point B1) indicates that ε_q can not fully recover in a closed elastic loading path. As observed in Fig. 2(c) and Fig. 2(d), the simulated elastic volumetric strain ε_v can completely recover (points C1 and C5 have the same ε_v value). Nevertheless, residual ε_q is observed in Fig. 2(b) and Fig. 2(c). The irreversible elastic deviatoric strain ε_q violates the description of the 'elasticity' theory and lacks the principle of energy conservation during a reversible process.

To amend such limitations, the hyperelasticity law proposed by Houlsby et al. (2019) is used in the upgraded SANISAND-MS model. The adopted hyperelasticity law suggests that stress σ can be rigorously derived from an elastic strain energy $\mathrm{E}(\varepsilon)$ by partial differentiate $\mathrm{E}(\varepsilon)$ with respect to the strain tensor: $\sigma = \partial \mathrm{E}(\varepsilon)/\partial\varepsilon$. The other equivalent form is that the strain tensor ε is a partial differential of complementary energy $\mathrm{C}\ (\sigma)$ with respect to the stress tensor: $\varepsilon = \partial \mathrm{C}(\sigma)/\partial\sigma$. The two forms can be related to each other by Legendre transform: $\mathrm{E}(\varepsilon) + \mathrm{C}(\sigma) = \sigma{:}\ \varepsilon$. Herein, the former was conducted.

The nonlinearity and anisotropy of soil were discussed independently by Houlsby et al. (2019). Amorosi et al. (2020) presented a simplified nonlinear anisotropic hyperelastic formulation with the switch parameter $N = 0$, which defines the datum point for stress at zero strain. However, the complete form of coupling the nonlinearity and anisotropy (i.e., using $N \neq 0$) is not presented in the two works

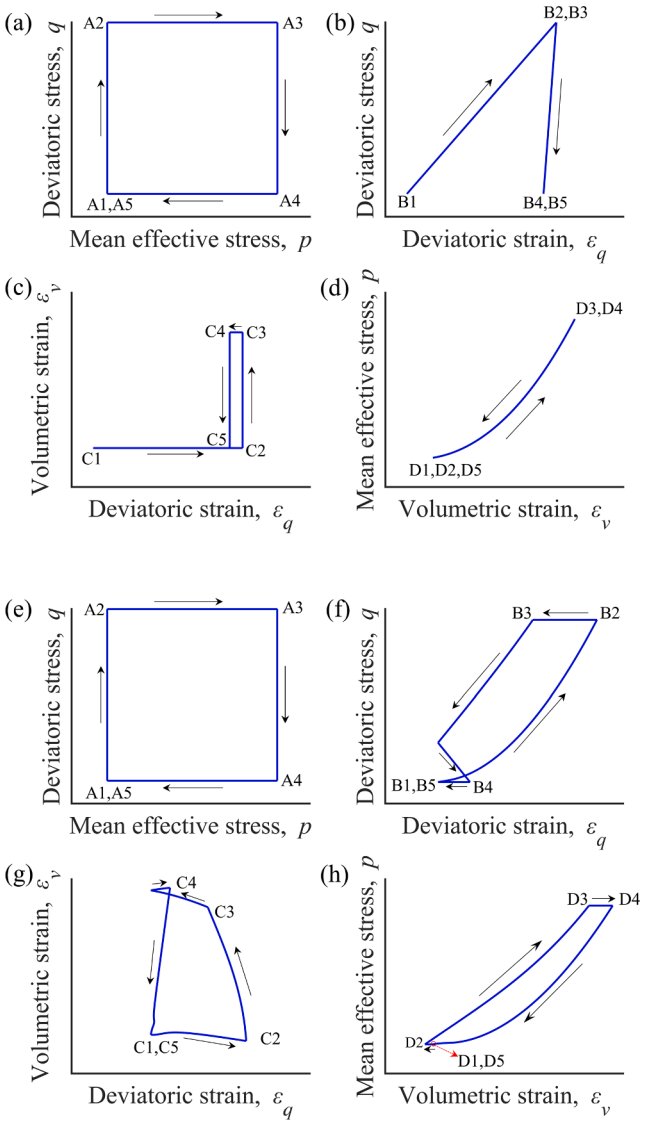

Fig. 2. Closed elastic stress path test under the same initial confining pressure and void ratio. Simulations with (a)~(d) hypoelastic model (Richart et al., 1970), (e)~(h) hyperelastic model (Houlsby et al., 2019).

mentioned above but is introduced in this section. The elastic strain energy function proposed by Houlsby et al. (2019) can be written in the general form:

$$E(\bar{\varepsilon}, \mathbf{a}) = \frac{P_r}{k(2-n)} \left[\frac{\bar{\varepsilon}^{2-n}}{r_0^{1-n}} - N\right] \tag{3}$$

Where P_r is an arbitrary reference pressure (for convenience, P_r is taken as the atmospheric pressure p_{at}, 101.3 kPa); k is a dimensionless bulk modulus; $0 \leq n < 1$ is a parameter controlling the nonlinearity dependence on pressure; $N = 1$ is adopted in this model; $\bar{\varepsilon}$ is the equivalent strain tensor that can be expressed by $\bar{\varepsilon} = \mathbf{a}\varepsilon\mathbf{a}$; $\mathbf{a}$ is a symmetric fabric tensor accounting for anisotropy of soil that stems from internal microstructural features (Lashkari, 2010; Amorosi et al., 2020; Mital et al., 2020). With the normalized method, i.e., set $\det(\mathbf{a}) = 1$, the fabric tensor $\mathbf{a}$ can be defined as:

$$a = \begin{bmatrix} y^{\frac{1}{3}} & 0 & 0 \\ 0 & y^{\frac{1}{3}} & 0 \\ 0 & 0 & y^{-\frac{2}{3}} \end{bmatrix} \tag{4}$$

where y^2 is equal to the shear modulus ratio G_{hh}/G_{vh} (assuming the 3rd axis is vertical direction). G_{hh} and G_{vh} are horizontal and vertical shear moduli which can be measured by bender element probing (Amorosi et al., 2020). The expression of y can be given as:

$$y = a_{11}/a_{33} \tag{5}$$

It is worth noting that Eq. (4) will reduce to the identity tensor which represents the isotropic elasticity while applying $y = 1$, without loss of generality.

In Eq. (5), a_{11} and a_{33} are the two diagonal values of the fabric tensor $\mathbf{a}$, which is an original form of Eq. (4) expressed as (Houlsby et al., 2019):

$$a = \begin{bmatrix} a_{11} & 0 & 0 \\ 0 & a_{22} & 0 \\ 0 & 0 & a_{33} \end{bmatrix} \tag{6}$$

Three diagonal eigenvalues of the fabric tensor $\mathbf{a}$ were employed to evaluate the diversity of soil inherent fabric in different directions. Nevertheless, for simplicity, only transverse anisotropy was considered (assuming the 3rd axis is vertical direction), where $a_{11} = a_{22} \neq a_{33}$, and the parameter y was applied in the upgraded SANISAND-MS model.

The term $\overline{r_0}$ in Eq. (3) is a positive root of Amorosi et al. (2020):

$$\overline{r_0}^2 = k(1-n)\left\{\left[k(1-n) - \frac{2}{3}g\right]\mathrm{tr}^2(\overline{\boldsymbol{\varepsilon}}) + 2g\mathrm{tr}(\overline{\boldsymbol{\varepsilon}}^{\mathrm{sym}^2})\right\} + N[N - 2k(1-n)\mathrm{tr}(\overline{\boldsymbol{\varepsilon}}) \tag{7}$$

Where $\overline{\varepsilon}^{\mathrm{sym}}$ is a symmetric equivalent strain tensor; g is the dimensionless shear modulus. The modulus k and g are related by Poisson's ratio ν as $\frac{g}{k} = \frac{3(1-2\nu)}{2(1+\nu)}$.

From the basic definition of hyperelasticity, the stress tensor can be obtained as:

$$\sigma = \frac{\partial \mathrm{E}(\overline{\varepsilon}, \mathbf{a})}{\partial \varepsilon} = \frac{\partial \mathrm{E}(\overline{\varepsilon}, \mathbf{a})}{\partial \overline{\varepsilon}} : \frac{\partial \overline{\varepsilon}}{\partial \varepsilon} \tag{8}$$

Further differentiate to Eq. (8), one can get the increment of stress tensor:

$$\dot{\sigma} = \frac{\partial \sigma}{\partial \varepsilon} : \dot{\varepsilon} = \left[\frac{\partial \overline{\varepsilon}}{\partial \varepsilon} : \frac{\partial^2 \mathrm{E}(\overline{\varepsilon}, \mathbf{a})}{\partial \overline{\varepsilon} \otimes \partial \overline{\varepsilon}} : \frac{\partial \overline{\varepsilon}}{\partial \varepsilon}\right] : \dot{\varepsilon} \tag{9}$$

Making differentiation to Eq. (3) with respective to $\overline{\varepsilon}$, it flows that:

$$\frac{\partial \mathrm{E}(\overline{\varepsilon}, \mathbf{a})}{\partial \overline{\varepsilon}} = \frac{P_r}{k(1-n)} \overline{r_0}^{\frac{1}{1-n}} \frac{\partial \overline{r_0}}{\partial \overline{\varepsilon}} \tag{10}$$

Further differentiation:

$$\frac{\partial^2 \mathrm{E}(\overline{\varepsilon}, \mathbf{a})}{\partial \overline{\varepsilon} \otimes \partial \overline{\varepsilon}} = \frac{P_r}{k(1-n)} \left(\frac{1}{1-n} \overline{r_0}^{\frac{n}{1-n}} \frac{\partial \overline{r_0}}{\partial \overline{\varepsilon}} \otimes \frac{\partial \overline{r_0}}{\partial \overline{\varepsilon}} + \overline{r_0}^{\frac{1}{1-n}} \frac{\partial^2 \overline{r_0}}{\partial \overline{\varepsilon} \otimes \partial \overline{\varepsilon}}\right) \tag{11}$$

Note the differential:

$$\frac{\partial \overline{\varepsilon}}{\partial \varepsilon} = \frac{\partial (\mathbf{a}\varepsilon \mathbf{a})}{\partial \varepsilon} = a \overline{\otimes} a \tag{12}$$

Differentiating Eq. (7) with respect to $\overline{\varepsilon}$, one can get the differential:

$$\frac{\partial \overline{r_0}}{\partial \overline{\varepsilon}} = \frac{k(1-n)}{\overline{r_0}} \left\{\left[k(1-n) - \frac{2}{3}g\right]\mathrm{tr}(\overline{\varepsilon})\mathbf{I} + 2g\overline{\varepsilon}^{\mathrm{sym}}\right\} - \frac{kN(1-n)\mathbf{I}}{\overline{r_0}} \tag{13}$$

Further differentiation to Eq. (13):

$$\frac{\partial^2 \overline{r_0}}{\partial \overline{\varepsilon} \otimes \partial \overline{\varepsilon}} = \frac{1}{\overline{r_0}} \left\{k(1-n)\left[k(1-n) - \frac{2}{3}g\right]\mathbf{I} \otimes \mathbf{I} + 2gk(1-n)\mathbf{I} \otimes \mathbf{I} - \frac{\partial \overline{r_0}}{\partial \overline{\varepsilon}} \otimes \frac{\partial \overline{r_0}}{\partial \overline{\varepsilon}}\right\} \tag{14}$$

Substituting Eq.(11)~(14) into Eq. (9), the elastic stiffness tensor $\mathbb{D}$ can be obtained as:

$$\mathbb{D} = \frac{P_r}{k(1-n)} a \overline{\otimes} a : \left(\frac{1}{1-n} \overline{r_0}^{\frac{n}{1-n}} \mathbf{A} \otimes \mathbf{A} + \overline{r_0}^{\frac{1}{1-n}} \mathbb{C}\right) : a \overline{\otimes} a \tag{15}$$

Where $\mathbf{A} = \frac{\partial \overline{r_0}}{\partial \overline{\varepsilon}}$ and $\mathbb{C} = \frac{\partial^2 \overline{r_0}}{\partial \overline{\varepsilon} \otimes \partial \overline{\varepsilon}}$, are given by Eq. (13) and Eq. (14), respectively.

The adopted hyperelasticity law guarantees the conservation of energy under a closed elastic stress path. As shown in Fig. 2(e)~(h), the same closed elastic loading path (A1)-(A2)-(A3)-(A4)-(A5) is simulated by the ***hyperelasticity*** law. Different from the ***hypoelasticity*** law, the soil response forms a closed loop for the corresponding q versus ε_q, ε_v versus ε_q and p versus ε_v (in that the initial and final states are identical) as depicted in Fig. 2(f), Fig. 2(g) and Fig. 2(h), respectively. This implies that there is no production or dissipation of energy under a close loop loading path, which proves the thermodynamic consistency of the hyperelasticity law. Such improvement mends the shortcomings of the hypoelasticity formulas adopted in the original SANISAND-MS model. This phenomenon has also been investigated and reported by Golchin et al. (2022). The upgraded SANISAND-MS model equations are summarized in Table 1.

The elasticity theory has been developed in the previous sections, the remaining of the upgraded SANISAND-MS model remains the same as that described by Liu et al., (2019), which will not be presented in this work for the sake of simplicity. All model parameters are briefly introduced in the third column of the table. The calibrations of the model parameters are discussed in the following sections.

2.2. Calibration of monotonic parameters

The model parameters of the upgraded SANISAND-MS can be divided into a monotonic subset (from n to n_d in Table 2) and a cyclic subset (from μ_0 to β in Table 2). The selection of the cyclic model parameters will not affect the model's monotonic performance as described by Liu et al. (2019).

For the monotonic subset, the parameters related to the hyperelasticity law, i.e., n, k, y and ν (additional two more compared to those used by the hypoelasticity law – G_0 and ν), need to be calibrated first according to the approach presented by Amorosi et al. (2020). To be specific, the elastic parameters can be calibrated based on the evolution of the shear elastic modulus and bulk modulus along a specific stress path. To achieve this, dynamic field techniques such as cross-hole tests or measurements with laboratory bender elements can be used. After the elasticity parameters are determined, the calibration of model parameters M to β as listed in Table 2 can be determined based on the laboratory element test results. The critical state related model parameters, which are expected to be directly informed by the laboratory test measured critical state line, need to be determined first. The plasticity model parameters n^b and n^d can be determined through the peak strength of the sand and the phase transformation state. The rest parameters belonging to the monotonic set need to be determined by trial and error to obtain the best match with, for example, a monotonic triaxial test. The required laboratory test type and parameter calibration procedure (including both the monotonic and cyclic sets of the model parameters) are described in detail by Liu et al. (2019) and Liu & Pisanò (2019). In this work, drained monotonic triaxial experimental data of Karlsruhe fine quartz sand carried out by Wichtmann (2005) are used to calibrate the monotonic subset model parameters. The calibrated model parameters are listed in Table 2. In Fig. 3, the simulation results using the upgraded SANISAND-MS model are compared with the original SANISAND-MS simulation results and the experimental results.

According to Fig. 3, the stress and strain response of the upgraded SANISAND-MS is in good agreement with the test data obtained by Wichtmann (2005) and the simulation results of Liu's et al. (2019). It indicates that the calibrated model parameters are representative to reproduce the monotonic behaviour of the Karlsruhe fine quartz sand.

Table 1
Formulas of the upgraded SANISAND-MS model.

	Constitutive equations	Material parameters
Elastic stiffness tensor	$\mathbb{D} = \frac{P_r}{k(1-n)}(\mathbf{a}\overline{\otimes}\mathbf{a}) : \left(\frac{1}{1-n}\frac{n}{\overline{r_0}\sqrt{1-n}}\mathbf{A}\otimes\mathbf{A} + \frac{1}{\overline{r_0}\sqrt{1-n}}\mathbb{C}\right) : (\mathbf{a}\overline{\otimes}\mathbf{a})$	ν Poisson ratio n nonlinearity parameter
	Eqs. (4)~(5) and (7) Eqs. (13)~(14)	k dimensionless bulk modulus y inherent anisotropy parameter
Critical state line	$e_c = e_0 - \lambda_c(p_c/p_{atm})^{\xi}$	e_0 reference critical void ratio λ_c, ζ CSL shape parameters
Yield function	$f = \sqrt{(\mathbf{s}-p\boldsymbol{\alpha}) : (\mathbf{s}-p\boldsymbol{\alpha})} - \sqrt{2/3}pm$	m yield locus opening parameter
Memory function	$f_m = \sqrt{(\mathbf{s}-p\boldsymbol{\alpha}^M) : (\mathbf{s}-p\boldsymbol{\alpha}^M)} - \sqrt{2/3}pm^M$	
Deviatoric plastic flow	$d\mathbf{e}^p = \langle L\rangle \mathbf{R}'$ $\mathbf{R}' = B\mathbf{n} - C[\mathbf{n}^2 - 1/3\mathbf{I}]$ $\mathbf{n} = (\mathbf{r}-\boldsymbol{\alpha})/(\sqrt{2/3}m)$ $B = 1 + 3(1-c)/(2c)\mathrm{g}(\theta)\cos 3\theta$ $C = 3\sqrt{3/2}(1-c)\mathrm{g}(\theta)/c$ $\mathrm{g}(\theta) = 2c/[(1+c) - (1-c)\cos 3\theta]$	
Volumetric plastic flow	$d\varepsilon_{vol}^p = \langle L\rangle D$ $D = \left[A_0\exp(\beta\langle\tilde{b}_d^M\rangle/b_{ref})\right](\mathbf{r}_\theta^d - \mathbf{r}) : \mathbf{n}$ $\mathbf{r}_\theta^d = \sqrt{2/3}\mathrm{g}(\theta)M\exp(n^d\Psi)\mathbf{n}$ $\tilde{b}_d^M = \left(\tilde{\mathbf{r}}_\theta^d - \tilde{\mathbf{r}}^M\right) : \mathbf{n}$ $b_{ref} = \left(\mathbf{r}_\theta^b - \mathbf{r}_{\theta+\pi}^b\right) : \mathbf{n}$ $\mathbf{r}_{\theta+\pi}^b = \sqrt{2/3}\mathrm{g}(\theta+\pi)M\exp(-n^b\Psi)(-\mathbf{n})$	A_0'intrinsic' dilatancy parameter β dilatancy memory parameter n^d void ratio dependence parameter
Yield surface evolution	$d\boldsymbol{\alpha} = (2/3)\langle L\rangle h(\mathbf{r}_\theta^b - \mathbf{r})$ $\mathbf{r}_\theta^b = \sqrt{2/3}\mathrm{g}(\theta)M\exp(-n^b\Psi)\mathbf{n}$ $h = \frac{b_0}{(\mathbf{r}-\mathbf{r}_{in}) : \mathbf{n}}\exp[\mu_0\left(\frac{p}{p_{atm}}\right)^{0.5}\left(\frac{b^M}{b_{ref}}\right)^2]$ $b_0 = gh_0(1-c_h e)/\sqrt{p_c/p_{atm}}$ $b^M = (\mathbf{r}^M - \mathbf{r}) : \mathbf{n}$	M critical stress ratio (triaxial compression) n^b void ratio dependence parameter c ompression-to-extension strength ratio h_0, c_h hardening parameters
Memory surface evolution	$dm^M = \sqrt{3/2}d\alpha^M : \mathbf{n} - (m^M/\zeta)f_{shr}\langle -d\varepsilon_{vol}^p\rangle$ $d\alpha^M = (2/3)\langle L^M\rangle h^M(\tilde{\mathbf{r}}_\theta^b - \tilde{\mathbf{r}}^M)$ $h^M = \frac{1}{2}[\frac{b_0}{(\mathbf{r}^M - \mathbf{r}_{in}) : \mathbf{n}} + \sqrt{\frac{3}{2}}\frac{m^M f_{shr}\langle -D\rangle}{\zeta(\mathbf{r}_\theta^b - \mathbf{r}^M) : \mathbf{n}}]$	μ_0 ratcheting parameter ζ memory surface shrinkage parameter

2.3. Calibration of the cyclic subset parameters

The calibrations of the cyclic subset of the model parameters are accomplished by the best-fitting of drained cyclic triaxial test results, particularly in the presence of anisotropic consolidation prior to shear cycling. The stress path of such tests can be sketched as Fig. 4(a) (along the denoted number: ①-②-③-④-⑤-③-④-⑤…), where q^{ampl} is cyclic amplitude, q^{ave} stands for cyclic average value, thus the average stress ratio η^{ave} can be defined as $\eta^{ave} = q^{ave}/p_{in}$.

Under the premise of the relatively small load ratio (i.e., under which condition the stress state does not enter the dilative regime), the influences of parameters ζ and β are negligible in drained loading cases according to Liu et al. (2019). The calibration procedure of ζ and β, which can be found in Liu et al. (2019), is out of the interest of the current work. The same values for ζ and β as in Liu et al. (2019) are adopted.

Table 2
Upgraded SANISAND-MS model parameters for Karlsruhe fine quartz sand and Toyoura sand.

Model features	Parameters	quartz sand	Toyoura sand
Elasticity	n	0.3	0.13
	ν	0.05	0.05
	k	330	680
	y	0.9	0.96
Critical state	M	1.27	1.25
	c	0.712	0.712
	λ_c	0.049	0.019
	e_0	0.845	0.934
	ξ	0.27	0.7
Yield surface	m	0.01	0.01
Plasticity modulus	h_0	1.54	1.008
	c_h	1.01	0.968
	n_b	1.95	1.1
Dilatancy	A_0	1.02	1.3
	n_d	1.05	4.5
Memory surface	μ_0	260	260
	ζ	0.0005	0.0005
	β	1	1

The calibration of μ_0 is accomplished by fitting the ratcheting response (or the accumulated strain ε^{acc} against the number of loading cycles N). ε^{acc} is defined as the accumulated total strain for the regular cycles using the following expression:

$$\varepsilon^{acc} = \sqrt{\frac{1}{3}\left(\varepsilon_{vol}^{acc}\right)^2 + \frac{3}{2}\left(\varepsilon_q^{acc}\right)^2} \tag{11}$$

where $\varepsilon_{vol}^{acc}, \varepsilon_q^{acc}$ are volumetric and deviatoric accumulated strain, respectively. The definition of the 'regular cycles' is given in Fig. 4(b).

Fig. 5 shows the simulation results of the upgraded SANISAND-MS model using different μ_0 values. The accumulated total strain decreases as the μ_0 value increases. $\mu_0 = 260$ allows the upgraded SANISAND-MS to give a good agreement with the test results (Wichtmann, 2005) and simulation results of the original SANISAND-MS (Liu et al., 2019). Figs. 2, 3 and 5 prove that the inclusion of a hyperelastic law into the original SANISAND-MS framework makes the model comply with physics law without worsening the behaviour of the original SANISAND-MS.

3. Performance of the upgraded SANISAND-MS model

3.1. Effects of the elasticity law on the undrained unloading response

The original and updated SANISAND-MS models use a narrow yield locus to represent the purely elastic behavior of sand – the onset of the sand behaviour upon unloading/reloading can be assumed and simulated within this range. The elastic range is controlled by the size of the yield surface through the yield surface parameter m. Larger m results in a larger elastic range. However, one may also consider adopting a zero-elastic range modelling approach within the same model framework, as presented by Dafalias and Taiebat (2016).

In the original SANISAND-MS, the adopted elasticity results in isotropic elasticity. Under undrained triaxial unloading, the tangent to the stress path in the elastic range is vertical by the original SANISAND-MS prediction, see the dash-dotted line in Fig. 6. Such a vertical tangent line disagrees with the observations from the experimental results, as has been pointed out by, e.g., Graham and Houlsby (1983), Verdugo and Ishihara (1996), Houlsby et al. (2005), Lashkari et al. (2021).

The hyperelasticity law adopted in the upgraded SANISAND-MS leads to an incrementally anisotropic elastic material behaviour. Such an adjustment of the elasticity law in the upgraded SANISAND-MS model reproduces the desired cross-coupling of the deviatoric and volumetric behaviour of sand as indicated by Amorosi et al. (2020). For

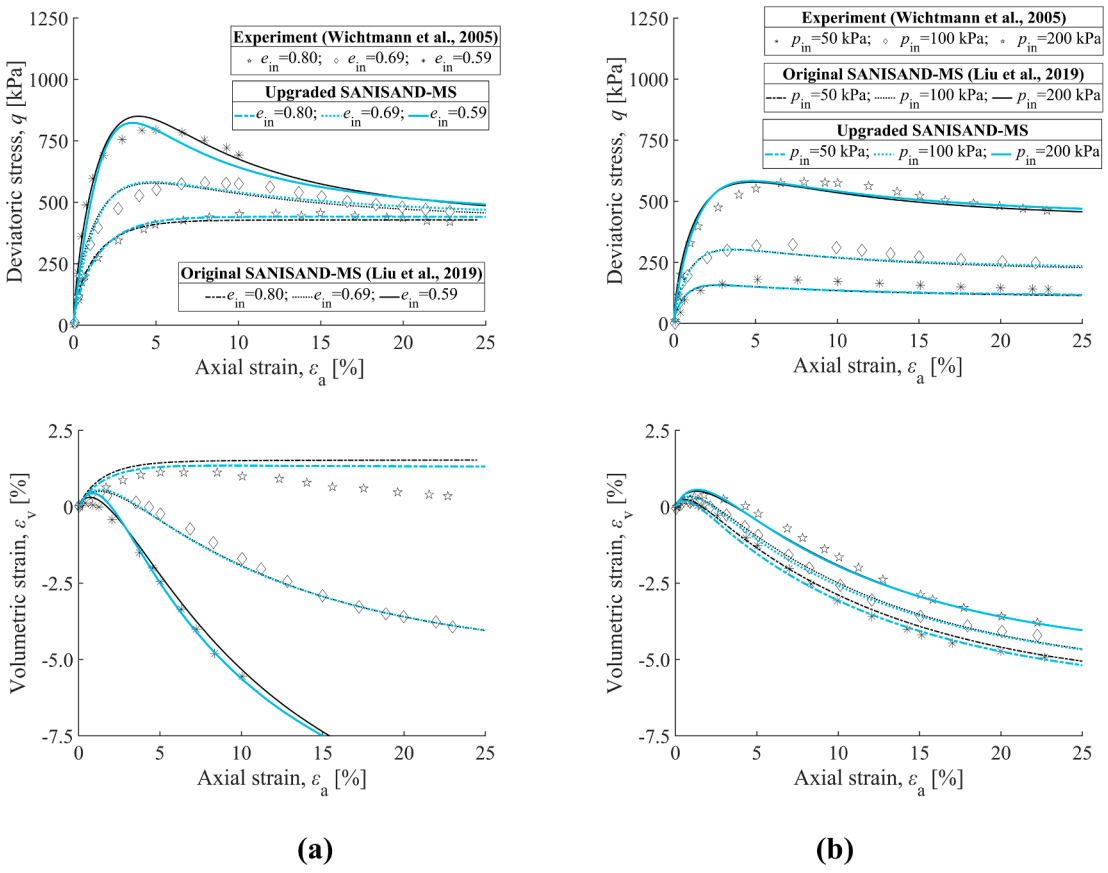

Fig. 3. Calibration of model parameters against the triaxial monotonic drained findings conducted by Wichtmann (2005), and compared with Liu's simulation results represented, (a) constant $p_{in} = 200$ kPa, varying e_{in}, (b) constant $e_{in} = 0.69$, varying p_{in}.

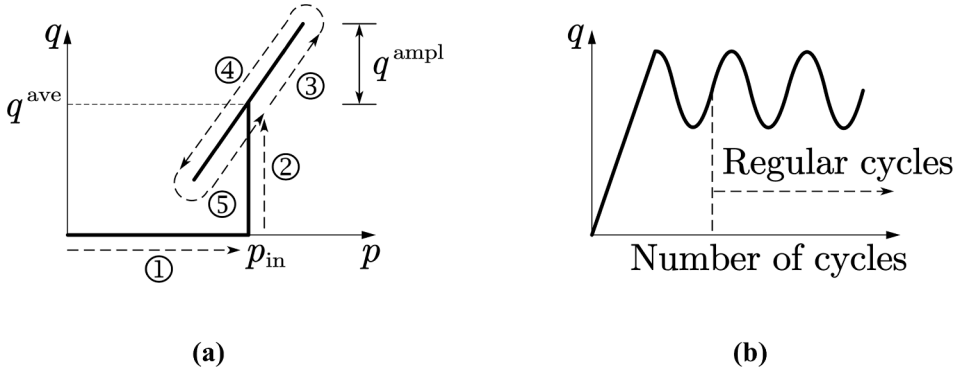

Fig. 4. Illustration of (a) stress path and (b) loading sequence considered in the cyclic test.

the same simulation in Fig. 6, the upgraded SANISAND-MS predicts a non-vertical tangent to the elastic part of the unloading path (the solid line in Fig. 6) – which matches the experimental observations at least at the qualitative level. In Fig. 6, simulations for the upgraded SANISAND-MS model using the parameters for Toyoura sand are listed in Table 2. The original SANISAND-MS model parameters of Toyoura sand are the same as those listed in Liu et al. (2019).

3.2. Effects of the inherent anisotropic parameter y

The direction of the undrained stress path at the onset of shearing is extensively affected by the sand's initial state. Reliable reproducing of sand undrained behavior requires the ability of the sand constitutive model to capture the feature. In the case of the Toyoura sand test result reported by Yang and Sze (2011), for instance, the undrained stress path moves directly in the direction of increasing effective stress p (see Fig. 7). Such behavior is not able to be captured by the original SANISAND-MS model. As mentioned, the original SANISAND-MS adopted isotropic elasticity and non-zero elastic range. The onset of the undrained shearing path predicted by SANISAND-MS always starts vertically. After that, the stress path biases towards the left (contractive) and then either continue to move towards the contractive side or starts moving towards the dilative side, depending on its relative state compared to the phase transformation state (see Fig. 7). The incorporation of the hyper-elastic law in the updated SANISAND-MS opens an opportunity to capture such behavior. Changing the direction of the onset stress path is achieved by varying the inherent fabric parameter y. For the example depicted in Fig. 7, adopting $y = 0.9$ provides the best fit

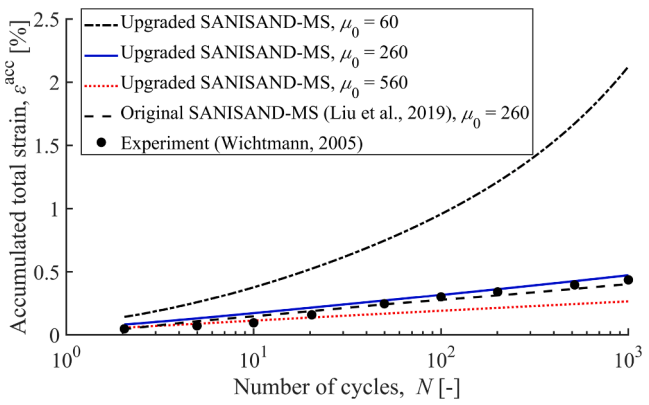

Fig. 5. Simulation curves of accumulated total strain varying with number of cycles for triaxial cyclic loading drained test compared with experiment (Wichtmann, 2005) and numerical results (Liu et al., 2019) following the settings: $e_{in} = 0.702$,$q^{ampl} = 60$ kPa, $p_{in} = 200$ kPa, $\eta^{ave} = 0.75$.

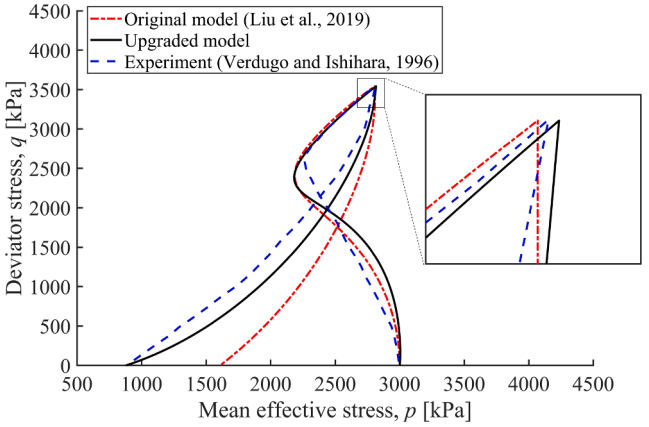

Fig. 6. Undrained triaxial stress path simulated with the original and upgraded SANISAND-MS on Toyoura sand. The simulations were performed under the settings: $p_{in} = 3000$ kPa, $e_{in} = 0.735$.

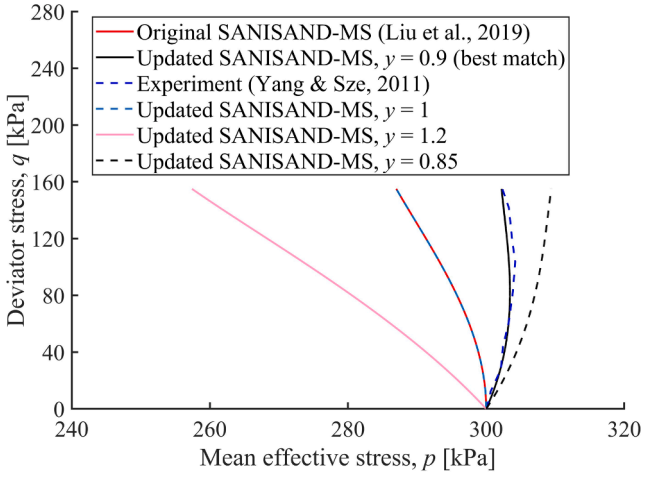

Fig. 7. Undrained monotonic triaxial test, the effect of the inherent anisotropic parameter y on the direction of stress path at the onset of shearing.

between the updated SANISAND-MS model and the experimental result.

The updated SANISAND-MS allows for adaptable control of the onset stress path direction (as shown by the different stress paths observed under various simulation conditions of y in Fig. 7). It is also worth noting that the updated SANISAND-MS can degrade to the original SANISAND-MS if $y = 1$ is used in conjunction with other equivalent settings for the elasticity parameters k and n.

It should be noted that in the current version of the model formulation, the inherent anisotropic feature is governed by the parameter y, without considering any evolution caused by the loading history. The anisotropy induced by the loading history can significantly affect the shearing behavior of the sand, as shown in Fig. 8(a). After being subjected to deviatoric preloading, the undrained stress path evolves towards the direction of increasing mean effective stress p (solid line). The evolution direction is opposite to the direction of the undrained stress path without deviatoric preloading (dashed line). Such distinct behavior cannot be captured through a single degree of anisotropy and principal directions of the fabric tensor (i.e., through a constant y). This is also demonstrated in Fig. 8 (b) and (c). No single y value can satisfactorily capture the stress paths under both conditions of with and without drained deviatoric preloading at the same time. One possible solution is to introduce a form of anisotropic elasto-plastic coupling (Golchin and Lashkari, 2014).

3.3. Performance of upgraded SANISAND-MS model in drained triaxial cyclic tests

The predictive capabilities of the upgraded SANISAND-MS model for drained cyclic loading are assessed by comparing the high-cycle triaxial test results reported by Wichtmann (2005) with the simulation results of the original SANISAND-MS model in this section.

Fig. 9 presents the effects of the initial confining pressure p_{in} on the sand ratcheting behaviour under the given load and soil conditions ($e_{in} = 0.684$, $\eta^{ave} = 0.75$, $q^{ampl}/p_{in} = 0.3$). The experimental data reveal that the initial p_{in} plays a minor role in the strain accumulation for the tested material and stress levels. However, the conclusion can be different for other test programs – see for instance Wichtmann et al., (2015). The upgraded SANISAND-MS model (Fig. 9(a)) performs similarly to the original SANISAND-MS model (Fig. 9(b)) and agrees well with the experimental results (Wichtmann, 2005).

Fig. 10 presents the influence of the initial void ratio on sand ratcheting behaviour. It indicates that the magnitude of the accumulated strain is greatly influenced by the initial void ratio. When subjected to the same load levels, loose sand accumulates larger strain at the same number of loading cycles. Such experimental evidence is reproduced by both the upgraded and the original SANISAND-MS models.

One should notice that, even though the void ratio was eliminated from the elasticity law of the original SANISAND-MS model when calculating the elastic stiffness tensor, the performance of the upgraded SANISAND-MS model regarding cyclic drained responses of sand under a variety of void ratios is satisfactory – the dependence of sand accumulated strain on the relative density is well captured by the upgraded model.

In Fig. 11, the simulation results from the upgraded and original SANISAND-MS models for cyclic tests with $q^{ampl} = 31$ kPa, 60 kPa and 80 kPa are presented and compared to the experimental results. Other loading and soil conditions are kept constant, as follows: $p_{in} = 200$kPa, $\eta^{ave} = 0.75$ and $e_{in} = 0.72$. The experimental and numerical results agree on the increased strain accumulation caused by increasing the amplitude of the cyclic stress.

3.4. Model performance under the low amplitude cyclic loading

Poblete et al. (2016) compared the experimental and simulation results of multidimensional cyclic loading tests, under low amplitude cyclic loading. In this section, low amplitude loading refers to stress states that do not exceed the yield surface. It concluded that the behaviour of sand is pseudo-elastic and that excessive irreversible strain should not be accumulated. From the constitutive modelling

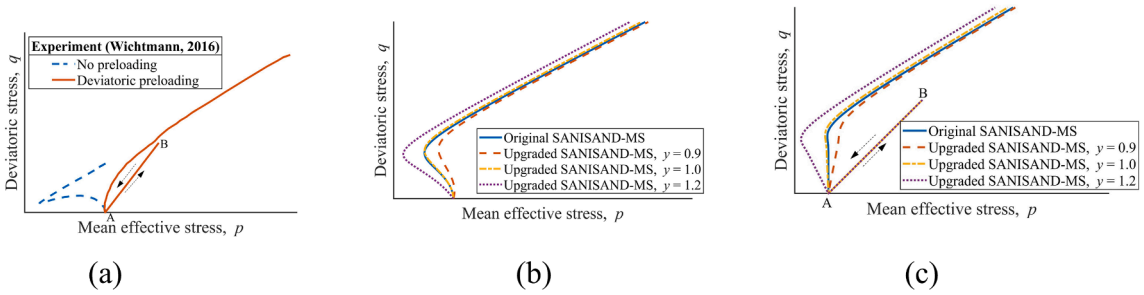

Fig. 8. Undrained monotonic triaxial test with and without drained deviatoric preloading, (a) experiment on Karlsruhe fine sand conducted by Wichtmann (2016), (b) simulation results for the case without drained deviatoric preloading and (c) simulation results for the case with drained deviatoric preloading.

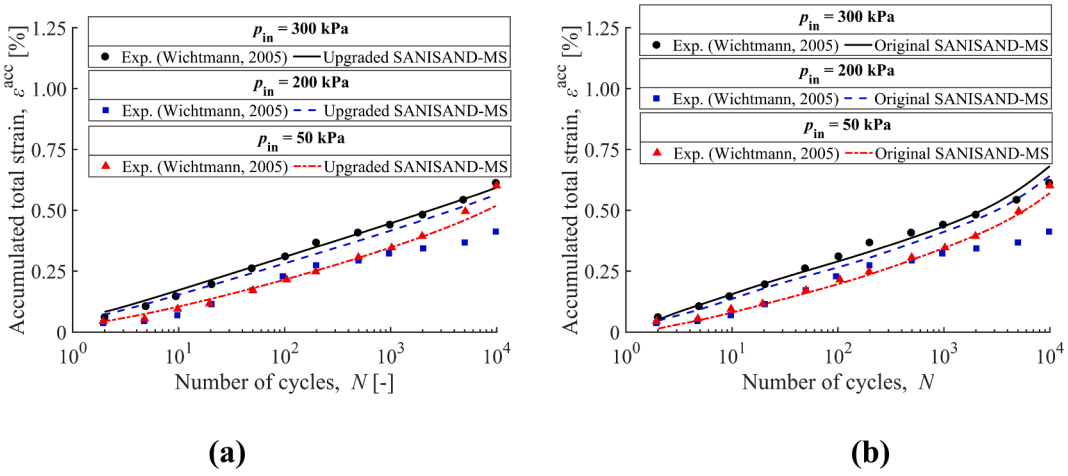

Fig. 9. Influence of initial mean pressures p_{in} on accumulated total strain curves compared with experimental data (Wichtmann, 2005), under the parameter settings: $e_{in} = 0.684$, $\eta^{ave} = 0.75$, $q^{ampl}/p_{in} = 0.3$; (a) the upgraded SANISAND-MS model, (b) the original SANISAND-MS (Liu et al., 2019).

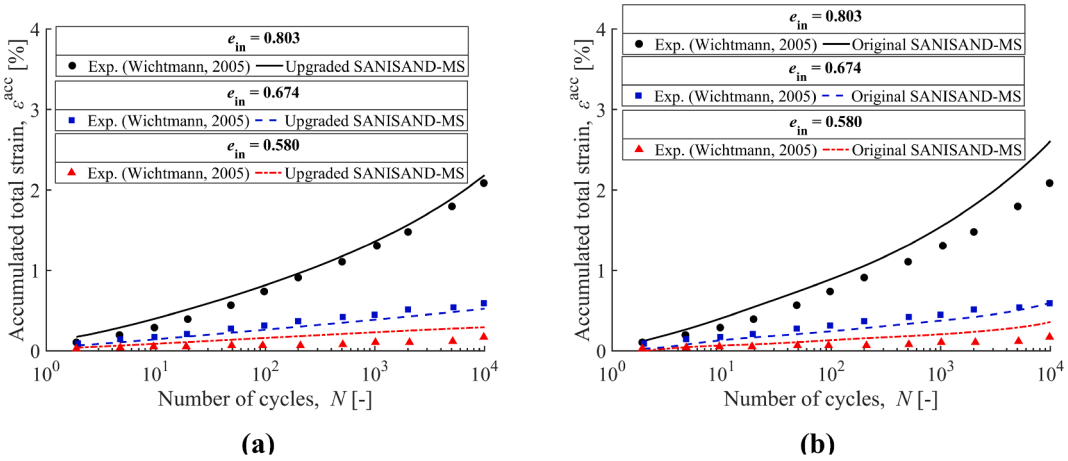

Fig. 10. Influence of the initial void ratios e_{in} on accumulated total strain curves compared with experimental data (Wichtmann, 2005), under the parameter settings: $p_{in} = 200$ kPa, $\eta^{ave} = 0.75$, $q^{ampl} = 60$ kPa; (a) the upgraded model, (b) the original model (Liu et al., 2019).

perspective, according to Duque et al. (2022), the artificial accumulation caused by the incorporation of hypoelasticity in the constitutive models is not negligible. To check this issue, simulations are conducted on the low amplitude of the drained cyclic test by the upgraded and original SANISAND-MS models. The tests were performed using the same model parameters as indicated in section 3.3 with the initial conditions: $p_{in} = 200$kPa, $e_{in} = 0.69$. The number of cycles $N = 10^4$ was considered. The closed low amplitude cyclic stress path and loading sequences are demonstrated in Fig. 12(a)-(b), respectively.

Under the condition of low amplitude cyclic loading, the responses of volumetric strain and deviatoric strain are presented in Fig. 13. As is shown in Fig. 13, the original SANISAND-MS model accumulates large values of deviatoric strain, while the upgraded SANISAND-MS manifests elasticity responses – which implies no irreversible strain is accumulated with the increase of cycles. Moreover, the deviatoric strain simulated by the original model shows an exponential increase with the increase of cycles. It can be predicted from the trends of the original model, if the number of cycles increases to a high level, a large residual irreversible

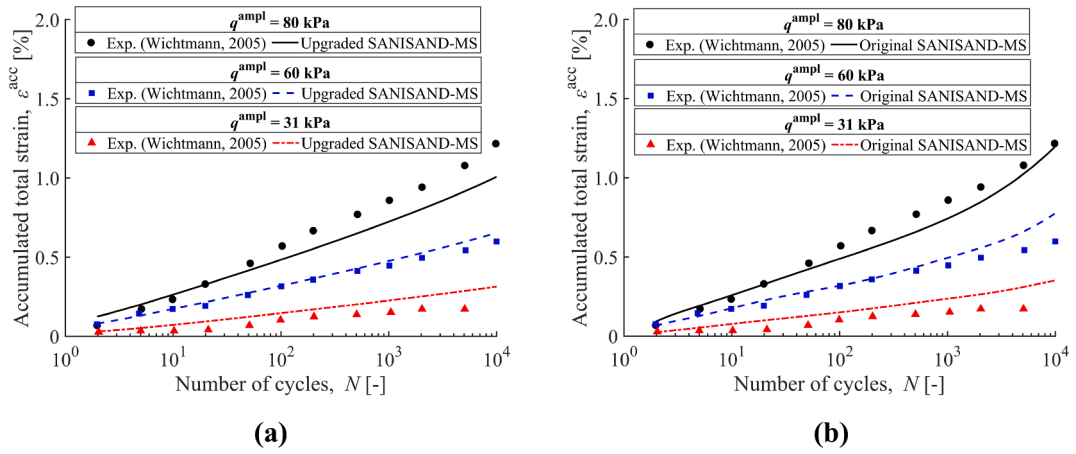

Fig. 11. Influence of the initial void ratios e_{in} on accumulated total strain curves compared with experimental data (Wichtmann, 2005), under the parameter settings: p_{in} = 200 kPa, η^{ave} = 0.75, e_{in} = 0.702; (a) the upgraded model, (b) the original model (Liu et al., 2019).

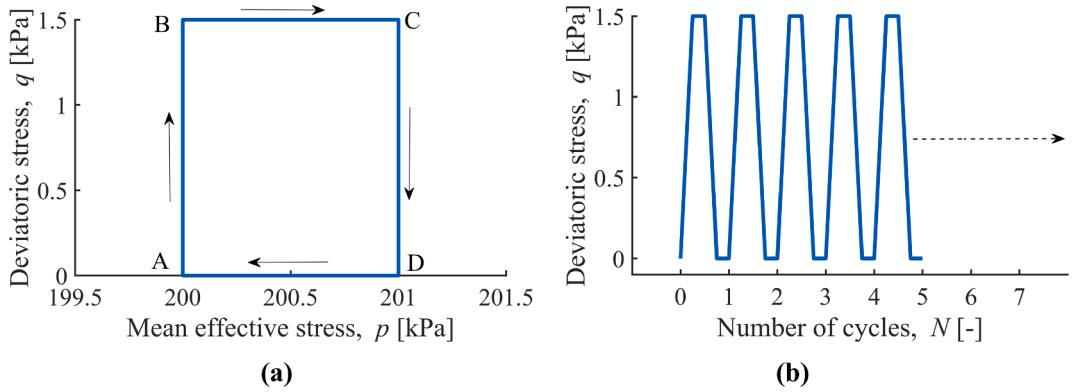

Fig. 12. Closed stress path for low amplitude drained cyclic loading tests. (a) $q \sim p$ stress path, (b) a part of loading sequences.

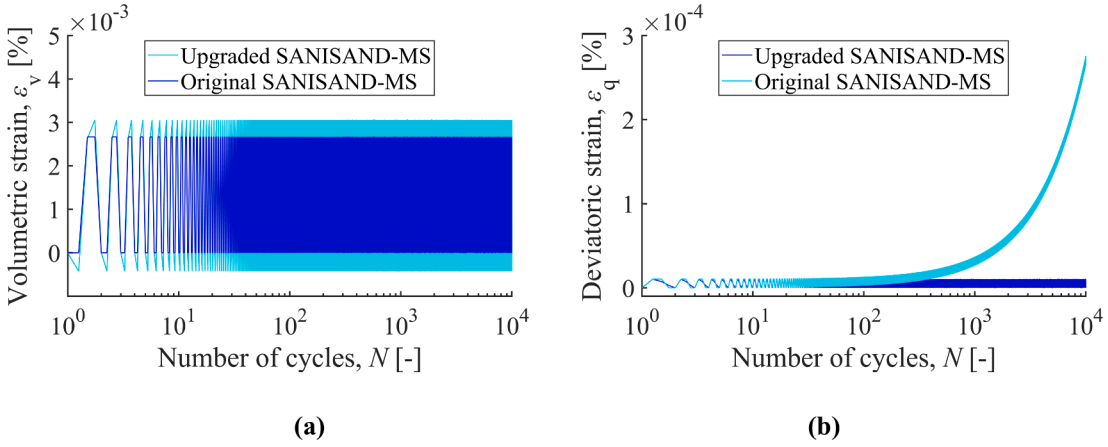

Fig. 13. Low amplitude drained cyclic loading tests under the settings: p_{in} = 200kPa, e_{in} = 0.69. (a) volumetric strain ~ number of cycles curve, (b) deviatoric strain ~ number of cycles curve.

strain can be accumulated even when subjected to a very low amplitude. As a result, one should be careful about the finite element calculation results when applying the original model to simulate realistic boundary problems – for example, simulating the soil-structure interaction of offshore wind turbine foundations under high cyclic wind or wave loads. Because it is in compliance with the first law of thermodynamics, the upgraded model is more accurate in predicting sand accumulation and is suitable for simulating problems with high-cyclic loads.

4. Conclusions

To avoid large spurious accumulated strain under high cyclic loading conditions, the hyperelasticity law was incorporated into the SANISAND-MS model by replacing the hypoelasticity law in the original model formulation. The complete form of the derived nonlinear elasticity functions enhanced by stress induced anisotropy is presented in this work. So as to ensure that the upgraded SANISAND-MS model can

account for a thermodynamically consistent formulation for its reversible response. The modification also aids in improving the model's ability to capture the small strain nonlinearity and anisotropic features of sand, which are of great importance in geotechnical applications. The upgraded SANISAND-MS model was implemented in the OpenSees platform, and the model parameters were calibrated using the trial and error method against the drained monotonic triaxial experimental data of Karlsruhe fine quartz sand. Simulation results for the unloading response show that the volumetric-deviatoric coupling effect makes the upgraded model more accurate at capturing stress-induced anisotropy during the initial unloading stage. The upgraded SANISAND-MS model also improves the capability of simulating the small amplitude cyclic behaviour of sand. The simulation results for the cyclic tests agree well with the experimental results and the original SANISAND-MS, completing a successful evaluation. The model is now ready for use in real boundary value problems that involve cyclic events, and it can reproduce more realistic sand high-cyclic behaviour.

CRediT authorship contribution statement

Hongjian Lan: Methodology, Data curation, Formal analysis, Software, Writing – original draft, Visualization. **Haoyuan Liu:** Conceptualization, Validation, Methodology, Writing – review & editing, Supervision, Software. **Hongfen Zhao:** Methodology, Validation, Writing – review & editing, Supervision, Funding acquisition.

Declaration of Competing Interest

The authors declare that they have no known competing financial interests or personal relationships that could have appeared to influence the work reported in this paper.

Acknowledgments

The financial contribution of the National Natural Science Foundation of China (No. 52279121; No. 52025094) is gratefully acknowledged. In addition, the authors would like to thank Dr. Federico Pisanò at Delft University of Technology for contributing to valuable discussions.

Data availability

Some or all data, models, or code generated or used during the study are available from the corresponding author upon reasonable request.

References

Amorosi, A., Rollo, F., Houlsby, G.T., 2020. A nonlinear anisotropic hyperelastic formulation for granular materials: comparison with existing models and validation. Acta Geotech. 15, 179–196. https://doi.org/10.1007/s11440-019-00827-5.

Cudny M., Partyka E., 2017. Influence of anisotropic stiffness in numerical analyses of tunneling and excavation problems in stiff soils. In: Lee W, Lee J-S, Kim H-K, Kim D-S (eds) Proceedings of the 19th international conference on soil mechanics and geotechnical engineering, Seoul 2017, International Society for Soil Mechanics and Geotechnical Engineering, Seoul, Korea, pp 719–722.

Dafalias, Y.F., Manzari, M.T., 2004. Simple plasticity sand model accounting for fabric change effects. J. Eng. Mech. 130, 622–634. https://doi.org/10.1061/(ASCE)0733-9399(2004)130:6(622).

Dafalias, Y.F., Taiebat, M., 2016. SANISAND-Z: zero elastic range sand plasticity model. Géotechnique 66 (12), 999–1013. https://doi.org/10.1680/jgeot.15.P.271.

Debnath, R., Saha, R., Haldar, S., 2022. Assessment of small strain dynamic soil properties of railway site Agartala, India, by bender element tests. Arab. J. Geosci 15, 1500. https://doi.org/10.1007/s12517-022-10749-4.

Duque, J., Yang, M., Fuentes, W., Mašín, D., Taiebat, M., 2022. Characteristic limitations of advanced plasticity and hypoplasticity models for cyclic loading of sands. Acta Geotech. 17, 2235–2257. https://doi.org/10.1007/s11440-021-01418-z.

Einav, I., 2012. The unification of hypo-plastic and elasto-plastic theories. Int. J. Solids Struct. 49, 1305–1315. https://doi.org/10.1016/j.ijsolstr.2012.02.003.

Einav, I., Puzrin, A.M., 2004. Pressure-Dependent Elasticity and Energy Conservation in Elastoplastic Models for Soils. J. Geotech. Geoenviron. Eng. 130, 81–92. https://doi.org/10.1061/(ASCE)1090-0241(2004)130:1(81).

Gajo, A., Bigoni, D., 2008. A model for stress and plastic strain induced nonlinear, hyperelastic anisotropy in soils. Int. J. Numer. Anal. Meth. Geomech. 32, 833–861.

Golchin, A., Lashkari, A., 2014. A critical state sand model with elastic–plastic coupling. Int. J. Solids Struct. 51 (15–16), 2807–2825.

Golchin, A., Vardon, P.J., Hicks, M.A., 2022. A thermo-mechanical constitutive model for fine-grained soils based on thermodynamics. Int. J. Eng. Sci. 174, 103579.

Graham, J., Houlsby, G.T., 1983. Anisotropic elasticity of a natural clay. Géotechnique 33 (2), 165–180.

Houlsby, G., Amorosi, A., Rojas, E., 2005. Elastic moduli of soils dependent on pressure: a hyperelastic formulation. Géotechnique 55, 383–392. https://doi.org/10.1680/geot.55.5.383.66021.

Houlsby, G.T., Amorosi, A., Rollo, F., 2019. Non-linear anisotropic hyperelasticity for granular materials. Comput. Geotech. 115, 103167 https://doi.org/10.1016/j.compgeo.2019.103167.

Kallehave, D., Thilsted, C.L., Liingaard, M., 2012. Modification of the API P-y formulation of initial stiffness of sand. Presented at the Offshore Site Investigation and Geotechnics: Integrated Technologies - Present and Future, pp. SUT-OSIG-12-50.

Korobeynikov, S.N., 2019. Objective symmetrically physical strain tensors, conjugate stress tensors, and hill's linear isotropic hyperelastic material models. J. Elast. 136, 159–187. https://doi.org/10.1007/s10659-018-9699-9.

Lashkari, A., 2010. A SANISAND model with anisotropic elasticity. Soil Dyn. Earthq. Eng. 30, 1462–1477. https://doi.org/10.1016/j.soildyn.2010.06.015.

Lashkari, A., Falsafizadeh, S.R., Rahman, M.M., 2021. Influence of linear coupling between volumetric and shear strains on instability and post-peak softening of sand in direct simple shear tests. Acta Geotech. 16, 3467–3488. https://doi.org/10.1007/s11440-021-01288-5.

Li, X., Dafalias, Y., 2001. Dilatancy for cohesionless soils - discussion. Géotechnique 51, 729–730. https://doi.org/10.1680/geot.51.8.729.40474.

Li, X.S., Dafalias, Y.F., 2002. Constitutive modeling of inherently anisotropic sand behaviour. J. Geotech. Geoenviron. Eng. 128 (10), 868–880.

Lin, R., 2003. Hypoelasticity-based analytical stress solutions in the simple shearing process. Z. Angew. Math. Mech. 83, 163–171. https://doi.org/10.1002/zamm.200310016.

Liu, H.Y., Abell, J.A., Diambra, A., Pisanò, F., 2019. Modelling the cyclic ratcheting of sands through memory-enhanced bounding surface plasticity. Géotechnique 69, 783–800. https://doi.org/10.1680/jgeot.17.P.307.

Liu, H.Y., Pisano, F., 2019. Prediction of oedometer terminal densities through a memory-enhanced cyclic model for sand. Géotechnique Letters 9 (2), 81–88.

Liu, H.Y., Diambra, A., Abell, J.A., Pisanò, F., 2020. Memory-enhanced plasticity modeling of sand behaviour under undrained cyclic loading. J. Geotech. Geoenviron. Eng. 146, 04020122. https://doi.org/10.1061/(ASCE)GT.1943-5606.0002362.

Liu, H.Y., Kaynia, A.M., 2021. Characteristics of cyclic undrained model SANISAND-MSu and their effects on response of monopiles for offshore wind structures. Géotechnique 1–16.

Mital, U., Kawamoto, R., Andrade, J.E., 2020. Effect of fabric on shear wave velocity in granular soils. Acta Geotech. 15, 1189–1203. https://doi.org/10.1007/s11440-019-00766-1.

Oh, K.-Y., Nam, W., Ryu, M.S., Kim, J.-Y., Epureanu, B.I., 2018. A review of foundations of offshore wind energy convertors: Current status and future perspectives. Renew. Sustain. Energy Rev. 88, 16–36. https://doi.org/10.1016/j.rser.2018.02.005.

Poblete, M., Fuentes, W., Triantafyllidis, T.h., 2016. On the simulation of multidimensional cyclic loading with intergranular strain. Acta Geotech. 11, 1263–1285. https://doi.org/10.1007/s11440-016-0492-2.

Richart, F.E., Hall, J.R., Woods, R.D., 1970. Vibrations of soils and foundations. International series in theoretical and applied mechanics, Prentice Hall, Englewood Cliffs, N.J.

Simo, J.C., Pister, K.S., 1984. Remarks on rate constitutive equations for finite deformation problems: computational implications. Comput. Methods Appl. Mech. Eng. 46, 201–215. https://doi.org/10.1016/0045-7825(84)90062-8.

Taiebat, M., Dafalias, Y.F., 2008. SANISAND: Simple anisotropic sand plasticity model. Int. J. Numer. Anal. Meth. Geomech. 32, 915–948. https://doi.org/10.1002/nag.651.

Tasiopoulou, P., Gerolymos, 2016. Constitutive modeling of sand: Formulation of a new plasticity approach. Soil Dynamics Earthquake Eng., 82, 205-221.

Verdugo, R., Ishihara, K., 1996. The steady state of sandy soils. Soils Found. 36, 81–91.

Vermeer, P.A., 1982. A five-constant model unifying well-established concepts. In: Gudehus, G., Darve, F., Vardoulakis, G. (Eds.), Results of the international workshop on constitutive relations for soils. Balkema, Grenoble, pp. 175–197.

Wichtmann, T., 2005. Explicit accumulation model for non-cohesive soils under cyclic loading. PhD thesis. Institut für Grundbau und Bodenmechanik, Bochum University, Bochum, Germany.

Wichtmann, T., 2016. Soil behaviour under cyclic loading-experimental observations, constitutive description and applications. Th, Triantafyllidis.

Wichtmann, T., Niemunis, A., Triantafyllidis, T., 2015. Improved simplified calibration procedure for a high-cycle accumulation model. Soil Dyn. Earthq. Eng. 70, 118–132. https://doi.org/10.1016/j.soildyn.2014.12.011.

Xiao, H., Bruhns, O.T., Meyers, A., 2005. Objective stress rates, path-dependence properties and non-integrability problems. Acta Mechanica 176, 135–151. https://doi.org/10.1007/s00707-005-0218-2.

Yang, J., Sze, H.Y., 2011. Cyclic behaviour and resistance of saturated sand under non-symmetrical loading conditions. Géotechnique 61 (1), 59–73.

Yao, Y.P., Hou, W., Zhou, A.N., 2009. UH model: three-dimensional unified hardening model for overconsolidated clays. Geotechnique 59 (5), 451–469.
Yao, Y.P., Liu, L., Luo, T., Tian, Y., Zhang, J.M., 2019. Unified hardening (UH) model for clays and sands. Comput. Geotech. 110, 326–343.
Zytynski, M., Randolph, M.F., Nova, R., Wroth, C.P., 1978. On modelling the unloading-reloading behaviour of soils. Int. J. Numer. Anal. Meth. Geomech. 2 (1), 87–93.